THE JOURNAL OF PHYSICAL CHEMISTRY C
A JOURNAL OF THE AMERICAN CHEMICAL SOCIETY

pubs.acs.org/JPCC

Article

Iridium-Doping as a Strategy to Realize Visible-Light Absorption and p-Type Behavior in $BaTiO_3$

Published as part of The Journal of Physical Chemistry C virtual special issue "The Physical Chemistry of Perovskites".

Sujana Chandrappa, Simon Joyson Galbao, P. S. Sankara Rama Krishnan, Namitha Anna Koshi, Srewashi Das, Stephen Nagaraju Myakala, Seung-Cheol Lee, Arnab Dutta, Alexey Cherevan, Satadeep Bhattacharjee, and Dharmapura H. K. Murthy*

Cite This: *J. Phys. Chem. C* 2023, 127, 12383−12393

Read Online

ACCESS | Metrics & More | Article Recommendations | Supporting Information

ABSTRACT: $BaTiO_3$ (BTO) typically demonstrates a strong n-type character with absorption only in the ultraviolet ($\lambda \leq 390$ nm) region. Extending the applications of BTO to a range of fields necessitates a thorough insight into how to tune its carrier concentration and extend the optical response. Despite significant progress, simultaneously inducing visible-light absorption with a controlled carrier concentration via doping remains challenging. In this work, a p-type BTO with visible-light ($\lambda \leq 600$ nm) absorption is realized via iridium (Ir) doping. Detailed analysis using advanced spectroscopy/microscopy tools revealed mechanistic insights into the n- to p-type transition. The computational electronic structure analysis further corroborated this observation. This complementary data helped establish a correlation between the occupancy and the position of the dopant in the band gap with the carrier concentration. A decrease in the Ti^{3+} donor-level concentration and the mutually correlated oxygen vacancies upon Ir doping is attributed to the p-type behavior. Due to the formation of Ir^{3+}/Ir^{4+} in-gap energy levels within the forbidden region, the optical transition can be elicited from or to such levels, resulting in visible-light absorption. This newly developed Ir-doped BTO is a promising semiconductor with imminent applications in solar fuel generation and optoelectronics.

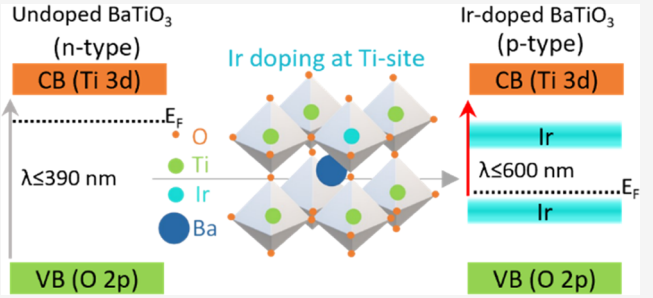

1. INTRODUCTION

Owing to their tunable properties, $ATiO_3$-type oxide perovskites (A = Ba, Sr, Ca) are promising materials with a range of applications in optoelectronics,[1] gas sensors,[2] transistors,[3] catalysis,[4,5] energy storage devices,[6] and photocatalysis.[7−9] Importantly, their performance is determined by their carrier concentration (n- or p-type), which depends on the ionic vacancies, doping, and defect chemistry/density.[10,11] $BaTiO_3$ (BTO), one of the widely known perovskite oxides, typically exhibits a strong n-type behavior (carrier concentration $\geq 10^{19}$ cm^{-3}).[12] Due to the size differences of Ba and Ti, BTO is highly susceptible to substitution/doping of various metal ions at both sites, thus offering a key tool to control its carrier concentration. In addition, the synthesis environment (reducing or oxidizing), ratio of precursors, and oxygen partial pressure significantly impact the carrier concentration and its optoelectronic properties.[13−16]

In the ideal stoichiometric $BaTiO_{3.0}$, the oxygen content and the total amount of metallic constituents (Ba^{2+} and Ti^{4+}) are chemically equivalent. Hence, BTO is expected to be an intrinsic semiconductor. However, owing to ubiquitous defects, as a result of synthesis conditions and/or (unintentional) doping, BTO is inherently nonstoichiometric ($BaTiO_{3\pm x}$). The defect equilibrium that renders a strong n-type behavior to BTO can be understood with the help of eqs 1 and 2. Under thermal equilibrium, owing to the inadequate oxygen, some Ti−O bond (lattice oxygen) dissociation takes place. This process releases molecular oxygen, leading to the formation of nonstoichiometric $BaTiO_{3-x}$, concurrently giving rise to oxygen vacancies as depicted in eq 1. Additionally, the oxygen vacancies are accompanied by free electrons, which are released into the host lattice (refer to eq 1) and can reduce Ti^{4+} ($3d^0$) to Ti^{3+} ($3d^1$), as indicated by eq 2. Such Ti^{3+} species are typically located close to the conduction band (CB) and act as donor levels,[17,18] which effectively increase the carrier

Received: May 4, 2023
Revised: June 1, 2023
Published: June 16, 2023

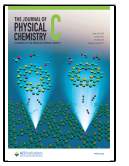

concentration. Therefore, the presence of Ti^{3+} levels in oxygen-deficient, nonstoichiometric $BaTiO_{3-x}$ renders a strong n-type behavior.[19]

$$BaTiO_3 = BaTiO_{3-x} + \frac{1}{2}xO_2 + 2xe^- + xV_0 \quad (1)$$

$$BaTiO_3 = BaTi(VI)_{1-2x}Ti(III)_{2x}O_{3-x} + \frac{1}{2}xO_2 + xV_0 \quad (2)$$

Among its many applications, BTO is also being used for solar fuel generation via photocatalysis. In this process, by virtue of its semiconducting behavior, charge carriers generated upon light absorption are used for reduction and oxidation reactions.[20] BTO has a wide optical band gap of ≈3.2 eV and is capable of absorbing the ultraviolet (UV) part of the solar spectrum. It is extensively utilized for photocatalytic solar fuel production, like its analogue, $SrTiO_3$.[21,22] Besides being chemically stable in aqueous conditions, the energetic positions of CB and VB offer thermodynamic driving energy to drive both reduction and oxidation of water. Another unique advantage of BTO is its ferroelectric behavior (in the tetragonal phase) that can be harnessed to enhance the charge photogeneration yield.[23,24] Recently, piezo-photocatalysis[25−27] has gained significant attention, wherein BTO-based materials hold promise toward cost-effective solar fuel production under ambient conditions.

The importance of carrier concentration in a photocatalyst (n- or p-type) on solar fuel efficiency has recently been established. The aluminum-doped $SrTiO_3$ photocatalyst has recently demonstrated ≈0.8% solar-to-hydrogen (STH) efficiency and remarkable stability, surpassing 200 days in 100 m^2 photocatalyst modules.[28] Note that to realize a high STH efficiency, Al^{3+} doping of $SrTiO_3$ was indispensable.[29] Interestingly, Al doping rendered p-type behavior to $SrTiO_3$ owing to Al^{3+} doping at the Ti^{4+} site, consequently decreasing the Ti^{3+} donor levels that contribute to the n-type behavior in $SrTiO_3$.[30,31] Thus, realizing a controlled transition between the n- and p-type nature is a promising strategy to enhance the photocatalytic H_2 evolution efficiency in oxide-based perovskites.

In the example discussed above, the Al^{3+} dopant did not form new defect levels within the forbidden region of the $SrTiO_3$ band gap. Thus, Al-doped $SrTiO_3$ retained virtually the same wide band gap (≈3.2 eV) as the undoped, absorbing light exclusively in the UV region that constitutes <5% of the solar spectrum. Besides inducing p-type behavior in photocatalysts, red-shifting the optical absorption to harness the visible region of the solar spectrum is essential. In this direction, very few reports show a p-type behavior with simultaneous band-gap narrowing via doping rhodium at Ti^{4+} sites of both $SrTiO_3$ and BTO.[32−34] Another important prospect of visible-light-absorbing p-type materials is to utilize them as photocathodes in the z-scheme in conjunction with n-type photoanode materials.[35−37] Rh-doped $SrTiO_3$ has been employed recently with molybdenum-doped $BiVO_4$ to achieve a remarkably high 1% STH efficiency.[36] Thus, there is a need for p-type photocatalysts that show promising photocatalytic activity under visible/near-infrared light.

Despite extensive research and prospects of BTO, only a very few visible-light-absorbing p-type BTO has been reported. Realizing visible-light absorption and a p-type BTO is not a straightforward process. This process demands a comprehensive understanding of the interplay between the number of mutually correlated and complex parameters, such as (i) the choice of dopant, (ii) site occupancy of dopant (Ba/Ti site) within the host lattice, (iii) the energetic position of the dopant energy levels within the forbidden region and its electron occupancy, and (iv) change in the electronic nature of the defects due to doping. All of these parameters collectively determine the carrier concentration and optical absorption properties. However, it has been challenging to understand the factors involved in realizing p-type and visible-light-absorbing BTO. In Rh-doped BTO, though the host and the dopant remain the same, different sites of occupancy were noticed. In one case, Rh was substituted for Ti sites, while in another case, Rh was substituted for Ba sites.[33,38] This observation indicates the complexity in predicting the electronic properties and the lack of comprehensive insight. There is immense scope to experimentally synthesize such a material for a wide range of applications.

In this work, we realized n- to p-type transition in BTO and extended its absorption toward the visible region ($\lambda \leq 600$ nm) through Ir doping at Ti sites. Doping-induced p-type behavior is rationalized based on the changes in the structural, surface, and optoelectronic properties using a range of complementary spectroscopy techniques and computational analysis of the electronic structure. A detailed mechanistic insight into the defect chemistry involved in p-type behavior is also provided. To the best of our knowledge, using Ir as a dopant to achieve p-type BTO is the first of its kind. This material will find promising applications in optoelectronics and photocatalysis.

2. EXPERIMENTAL SECTION

Barium nitrate (99%, Merck), titanium(IV) oxide nanopowder (NanoArc. anatase 99%, Alfa Aesar), and iridium(IV) oxide (99.9%, Aldrich) were used for synthesis without any further treatment. Undoped $BaTiO_3$ (undoped BTO) and Ir-doped $BaTiO_3$ (Ir-doped BTO) were synthesized using the solid-state reaction method. Stoichiometric amounts of $Ba(NO_3)_2$ (261.35 mg) and TiO_2 (79.9 mg) were ground using an agate mortar and pestle for 45 min. The mixture was transferred into an alumina boat crucible and was calcined at 900 °C for 12 h at a 10 °C min^{-1} ramp rate. The obtained product was named undoped BTO. For Ir-doped BTO synthesis, the IrO_2 amount corresponding to 3 mol % doping was ground in an agate mortar with $Ba(NO_3)_2$ and TiO_2 for 45 min, followed by calcination at 900 °C for 12 h at a 10 °C min^{-1} ramp rate. To ensure data comparison between these two samples, the precursors for undoped and Ir-doped BTO were ground and calcined separately by maintaining the exact same temperature conditions (target temperature, hold time, ramp rate, gas environment) mentioned above.

The powder X-ray diffraction was performed using a Bruker D_2 Phaser using Cu Kα radiation as the radiation source of wavelength λ = 1.54 Å. The samples were mounted on the sample holder, and the XRD pattern was recorded from 20 to 90° 2θ with a 0.02° step size and a scan speed of 0.3 s per step.

Transmission electron microscopy (TEM) and scanning transmission electron microscopy (STEM) studies were performed using aberration-corrected JEOL ARM 200 CF operated at 200 keV. The STEM probe size and the collection semiangle range are 90 pm and 140−200 mrad, respectively. STEM-energy-dispersive X-ray spectroscopy (STEM-EDS) mapping was performed using an Oxford SDD detector. The

https://doi.org/10.1021/acs.jpcc.3c02942
J. Phys. Chem. C 2023, 127, 12383−12393

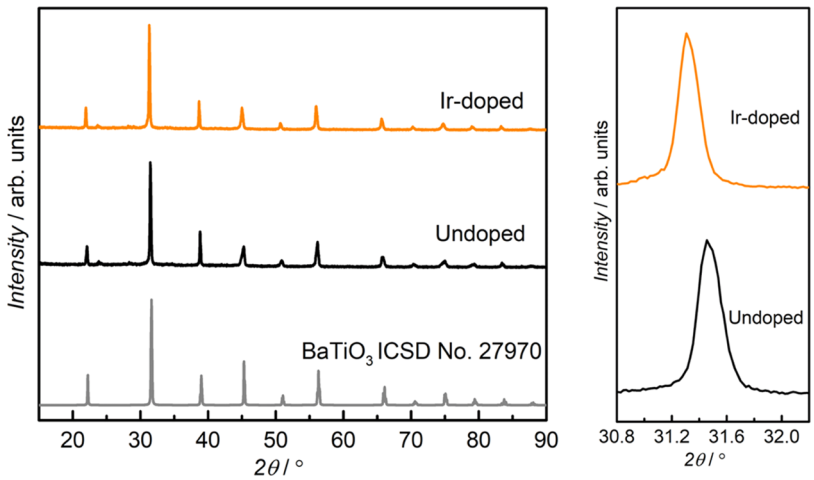

Figure 1. XRD patterns of undoped and Ir-doped BTO powder samples.

samples for TEM/STEM studies were prepared by the drop-casting method. The powder samples were dissolved in isopropyl alcohol and sonicated for 120 min. Using a dropper, the required amount of sample liquid was extracted and cast on a gold-coated lacey carbon grid. The drop-cast sample was left overnight in air for drying.

The optical absorption of the samples was measured using a PerkinElmer lambda 750 UV/vis/NIR spectrometer in the diffuse reflectance mode equipped with an integrating sphere.

Valence states and surface properties of the constituting elements were investigated by X-ray photoelectron spectroscopy (XPS) using a Thermo-Scientific NEXSA spectrometer, which uses Al Kα (1486.6 eV) as the X-ray source. The operating pressure in the ultrahigh vacuum range was from 10^{-8} to 10^{-10} mbar. The XPS survey spectra were recorded at the pass energy of 200 eV with a step size of 1 eV. The XPS higher energy resolution spectra were recorded with a pass energy of 50 eV with a step size of 0.1 eV. A flood gun was used to eliminate the charging effects. The spectral charge correction was performed using carbon with the C 1s peak appearing at 284.8 eV. Ultraviolet photoelectron spectroscopy (UPS) or valence band-XPS (VB-XPS) experiments were performed using the spectrometer Thermo-Scientific NEXSA with the He I (21.22 eV) excitation source. The pass energy used was 2 eV with a 0.050 eV step size. The operating pressure in the ultrahigh vacuum range was from 10^{-8} to 10^{-10} mbar. VB spectra of undoped and Ir-doped BTO were plotted by converting the counts vs kinetic energy (eV) to counts vs binding energy (eV). Conversion of kinetic energy to binding energy was performed considering the following equation: photon energy = binding energy + kinetic energy provided the spectrometer is calibrated such that the Fermi energy will appear at binding energy zero.

Electron paramagnetic spectroscopy (EPR) analysis was performed using the JOEL Model JES FA200 spectrometer. X-band EPR spectral analysis was performed at 77.3 K using a microwave frequency of 9.13 GHz, a microwave power of 1.0 mW, and a modulation frequency of 100 kHz.

Electrodes for the photoelectrochemical measurements were prepared as follows. 2.0 mg of Ir-doped BTO was added to the solution containing 160 μL of ethanol, 40 μL of distilled water, and 10 μL of Nafion, which was sonicated for 45 min to prepare the inks. The working electrode was prepared by drop-casting 20 μL of the prepared ink on the ITO (indium tin oxide)-coated glass substrate of 0.25 cm^2 area and drying under an infrared lamp. Photoelectrochemical measurements were recorded using a Metrohm Autolab PGSTAT 204 potentiostat using the three-electrode system, with platinum as the counter electrode, Ag/AgCl as the reference electrode, and ITO-coated glass substrates as the working electrode. K_2SO_4 was used as the supporting electrolyte, and the photoelectrochemical measurements were recorded at the scan rate of 5 mV s^{-1} with a 40 W Kessil KSPR160L LED of 427 nm.

The effect of Ir doping on the electronic structure of BTO was investigated computationally using density functional theory (DFT) implemented in the Vienna ab initio simulation package (VASP).[58−60] Here, the electron−ion interactions are treated using the projector augmented wave (PAW) method.[61] The generalized gradient approximation (GGA) with the Perdew−Burke−Ernzerhof (PBE)[62] functional is used for electron exchange-correlation effects. The calculations are carried out with a cutoff energy of 500 eV. The Brillouin zone of the supercell is sampled using Monkhorst−Pack k-point grids of 3 × 3 × 3 and 7 × 7 × 7 for self-consistent and non-self-consistent field calculations, respectively.[63] The convergence criterion for the total energy is 10^{-6} eV, and the residual force on each atom is less than 0.01 eV A^{-1} in the relaxed structure. In a 3 × 3 × 3 supercell of BTO, there are 27 Ba atoms, 27 Ti atoms, and 81 oxygen atoms as shown in Figure S6a. However, by virtue of the inherent oxygen-deficient nature of BTO, the oxygen deficiency is incorporated in both undoped and Ir-doped BTO (refer Figure S6a,b). The density of states (DOS) of pristine BTO was calculated, and it is found that the band gap is underestimated, which is the norm of GGA for semiconductors. Next, a rotationally invariant approach of GGA + U[64] is employed, where U values of 4 and 8 eV are used for Ti and O, respectively, and these are taken from an earlier report.[65] With this set of values, the band gap of BTO is 2.3 eV, less than what is experimentally reported. By taking U_{Ti} and U_O to be 8 and 8 eV, respectively, the band gap increases to 2.9 eV, which is still lower than the reported experimental value. Since we are interested in qualitative changes, we stick to the commonly used U_{Ti} = 4 eV and U_O = 8 eV, and for Ir, a U value of 2 eV is considered.

3. RESULTS AND DISCUSSION

Doping-induced changes in carrier concentration reflect a change in the structural, surface, and optoelectronic properties

https://doi.org/10.1021/acs.jpcc.3c02942
J. Phys. Chem. C 2023, 127, 12383−12393

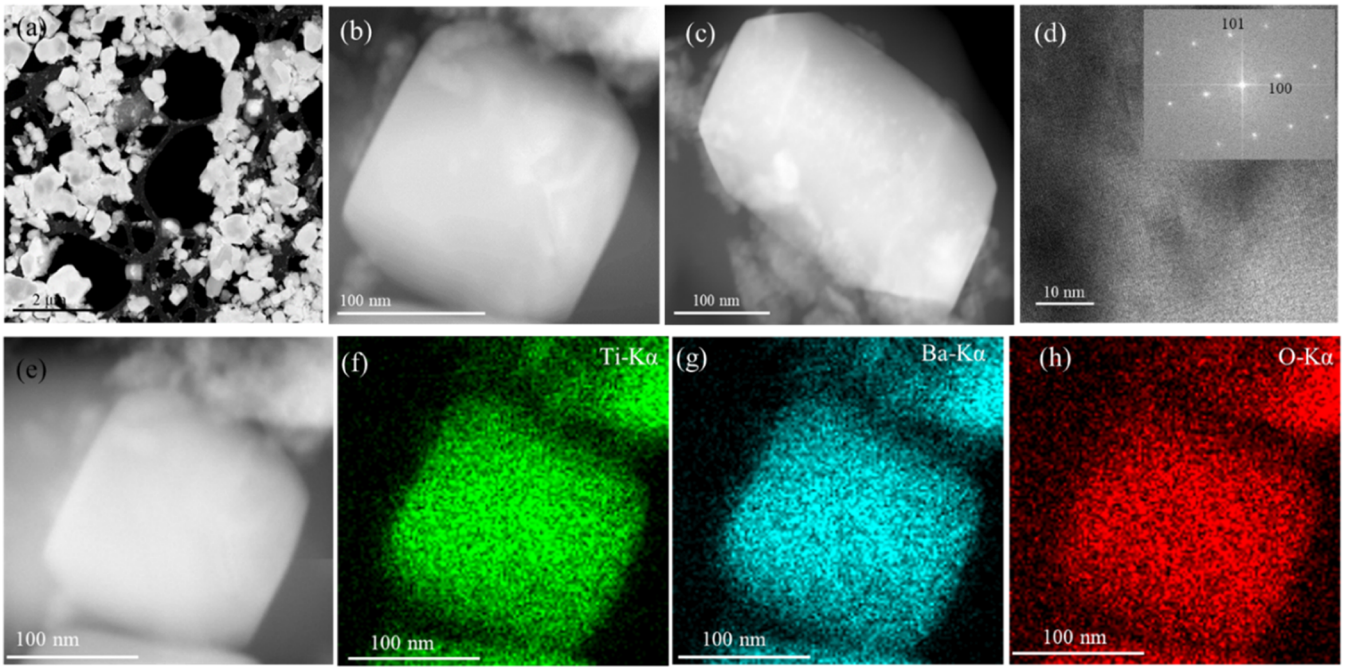

Figure 2. (a–c) STEM-HAADF images. (d) TEM bright-field image with SAD pattern and FFT inset. (e–h) STEM-EDS image and mapping corresponding to Ti (f), Ba (g), and O (h).

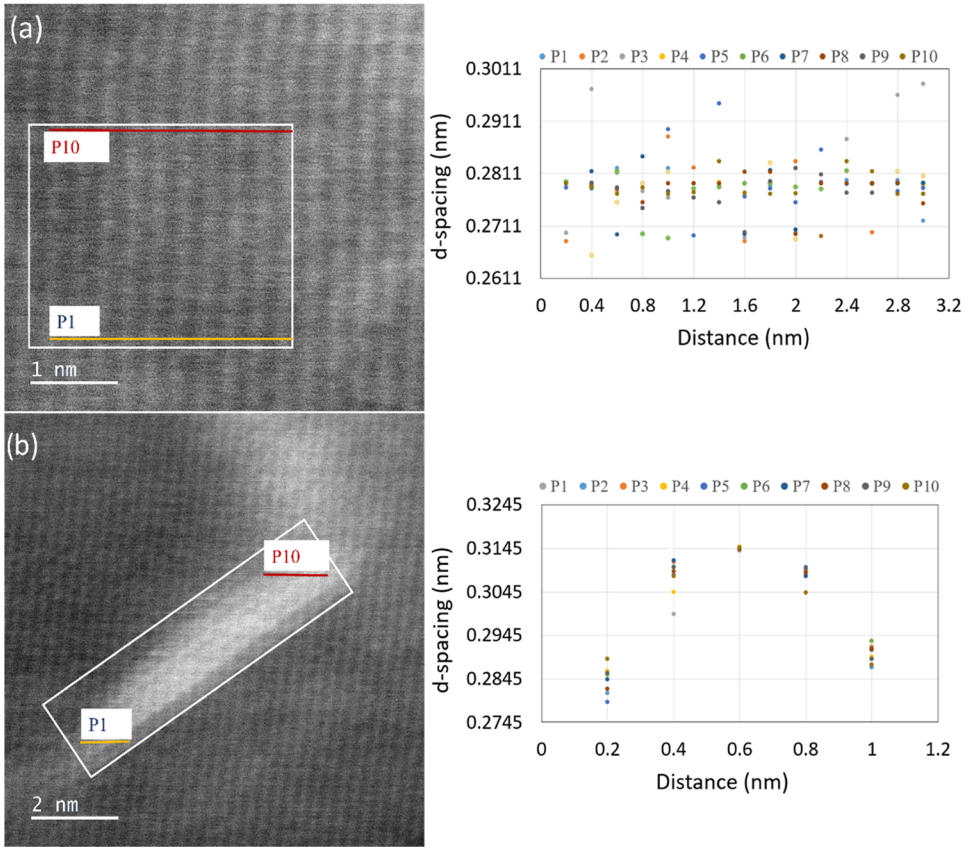

Figure 3. STEM-HAADF image of Ir-doped BTO showing the (a) pristine region and (b) doped region along with its *d*-spacing values recorded over 10 lattice points.

and are strongly dependent on the site of occupancy of the Ir in $BaTiO_3$. In this direction, probing the site of occupancy (Ti^{4+} site or Ba^{2+} site) of Ir is essential and will constitute the first part of the Results and Discussion section. This part would aid in explaining the origin of visible-light absorption and p-type behavior upon Ir doping, which will be examined in Section 3.2.

https://doi.org/10.1021/acs.jpcc.3c02942
J. Phys. Chem. C 2023, 127, 12383−12393

3.1. Determining the Site of Occupancy. Figure 1 presents the XRD patterns of the synthesized undoped BTO and Ir-doped BTO. Both samples show peaks characteristic of the BTO cubic phase, according to the ICSD database (ICSD No. 27970). Owing to the susceptibility of the BTO structure to doping at both the Ba site and the Ti site, determining the site of occupancy of Ir in the BTO host lattice is rather difficult. The ionic radii of Ba^{2+}, Ti^{4+}, and Ir^{4+} are 161, 60.5, and 75.6 pm, respectively. Solely based on the ionic radii values, Ir^{4+} is expected to substitute for a bigger sized Ba^{2+} site, which would result in lattice contraction, leading to the shift of XRD peaks toward higher 2θ values. On the contrary, compared to undoped BTO, a 2θ shift of around 0.16° is observed toward lower values for Ir-doped BTO, hinting at lattice expansion. Additionally, the calculated average lattice parameter of undoped BTO is 0.4016 nm, which is in agreement with that of undoped BTO reported earlier.[39] After Ir doping, the average lattice parameter increases to a value of 0.4033 nm (Tables S1 and S2), indicating lattice expansion. This observation can only be explained by the fact that the Ir dopant occupies the Ti^{4+} site. With Ir^{4+} occupying the Ti^{4+} site at the body-centered cubic (bcc) position in TiO_6 octahedra of the BTO lattice, the difference in ionic radii would lead to structural distortion, resulting in lattice expansion.

Figure 2a–c shows the STEM-HAADF (high-angle annular dark field) images of undoped BTO. In addition to the random distribution of particles, two distinct morphologies of powder samples are observed. Square particles of size ~80–100 nm and rectangle particles of size ~200 nm are observed (b and c), and both morphologies show a very uniform bright contrast, confirming the uniform distribution of Ba, Ti, and O. The TEM bright-field image (Figure 2d) shows a uniformly distributed lattice, and in the inset, fast Fourier transform (FFT) confirms the cubic phase of undoped BTO, which is in agreement with the XRD data in Figure 1. STEM-EDS mapping of Ba, Ti, and O in Figure 2e–h shows a very distinct contrast of each element, indicating the uniform distribution of elements.

The influence of Ir doping on structural modification in the BTO lattice was further analyzed. STEM-HAADF images in Figure S1a,b indicate spherical and rectangular morphologies with dimensions on the order of ~50 nm. STEM-EDS mapping presented in Figure S1e–h indicates a distinct contrast between Ba, Ti, O, and Ir elements, evidencing their uniform distribution. This observation rules out the possibility of Ir segregation or phase separation in the doped sample. Figure 3a,b presents the STEM-HAADF images of Ir-doped BTO showing pristine and doped regions, respectively. Dark and bright contrast confirms the presence of pristine and Ir-doped regions, respectively.[40,41] The contrast in STEM-HAADF images is observed due to the differences in the atomic number, and the bright contrast observed in this sample arises due to the presence of Ir as it is heavier than Ba and Ti. The bright contrast extends over a few unit cells, thereby confirming that the distribution of Ir is highly localized, which is expected for a relatively low 3 mol % dopant level. The white box in Figure 3a,b represents the region considered for the calculation of interplanar spacing (d-spacing) with 10 lattice positions (P1–P10) considered along the x-axis. The pristine region in Figure 3a has an average lattice parameter of 0.2792 nm, which closely matches with the d-spacing of the (101) plane, deduced from XRD analysis (refer to Tables S1 and S2). If the Ir dopant is substituted for the relatively bigger Ba site, the d-spacing is expected to decrease owing to lattice contraction. However, the observed average lattice parameter of the Ir-doped region in Figure 3b is 0.3146 nm, which is higher by 0.035 nm compared to the pristine region (Figure 3a). This observation indicates a lattice expansion that is in agreement with the XRD results discussed earlier. This increase in the d-spacing due to Ir doping is justifiable only by considering Ir doping at the relatively smaller Ti sites of the BTO lattice resulting in lattice expansion. Furthermore, HR-TEM analysis (Figure S1c) also demonstrated a structural modification in the TiO_6 octahedral orientation due to doping from (200) to (202).[42,43] This observation further corroborates Ir doping at the Ti site. Therefore, bulk (XRD) and atomic-level (TEM) analyses of the doping-induced structural changes collectively inferred the occupation of Ir at the Ti site of the BTO lattice.

To further understand the defect chemistry on doping, the surface chemical state of various constituent elements of BTO is investigated by XPS. Figure 4 depicts the Ir 4f spectra of Ir-doped BTO. The Ir 4f spectral deconvolution yielded a full width at half-maximum (FWHM) of 1.75. The characteristic Ir $4f_{7/2}$ peak is reported to appear between 62.3 and 62.8 eV for Ir in the 4+ oxidation state and between 61.6 and 62.0 eV for Ir in the 3+ oxidation state.[44–46] The binding energy of Ir $4f_{7/2}$ at 62.8 eV (indicated by orange) corresponds to that of Ir^{4+}, while that at 61.7 eV (indicated by violet) can be attributed to Ir^{3+}. The relative percentage of Ir^{4+}/Ir^{3+} is 1.68, which evidences that the Ir dopant in the BTO host exists predominantly as Ir^{4+}.

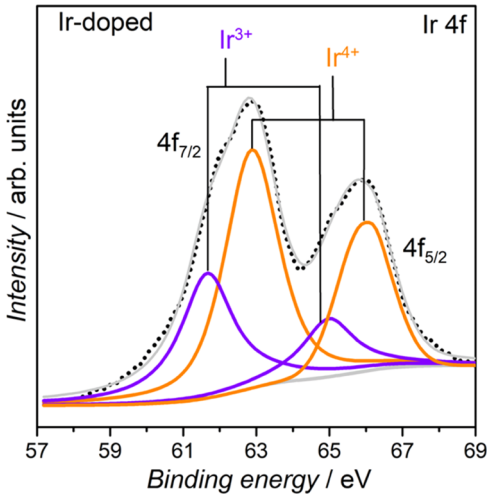

Figure 4. High-resolution XPS core-level spectrum of Ir-doped BTO showing the Ir 4f region.

To elucidate the changes in the chemical state(s) of Ti species on Ir doping, Ti 2p core-level spectra were analyzed in detail. Figure 5a,b depicts the Ti 2p spectra of undoped and Ir-doped BTO, respectively. To obtain the best fit for Ti 2p spectra of both samples, deconvoluting the spectra into three components was essential, indicating the presence of Ti in three different oxidation states. Table 1 lists the fitting parameters and individual contributions from Ti^{4+}, Ti^{3+}, and Ti^{2+} before and after doping. In undoped BTO, observing a characteristic doublet at 458.3 eV ($2p_{3/2}$) and 464.0 eV ($2p_{1/2}$) indicated the presence of Ti^{4+}.[47] Besides, pronounced peaks at 457.1 eV ($2p_{3/2}$) and 462.8 eV ($2p_{1/2}$) are attributed to the

https://doi.org/10.1021/acs.jpcc.3c02942
J. Phys. Chem. C 2023, 127, 12383–12393

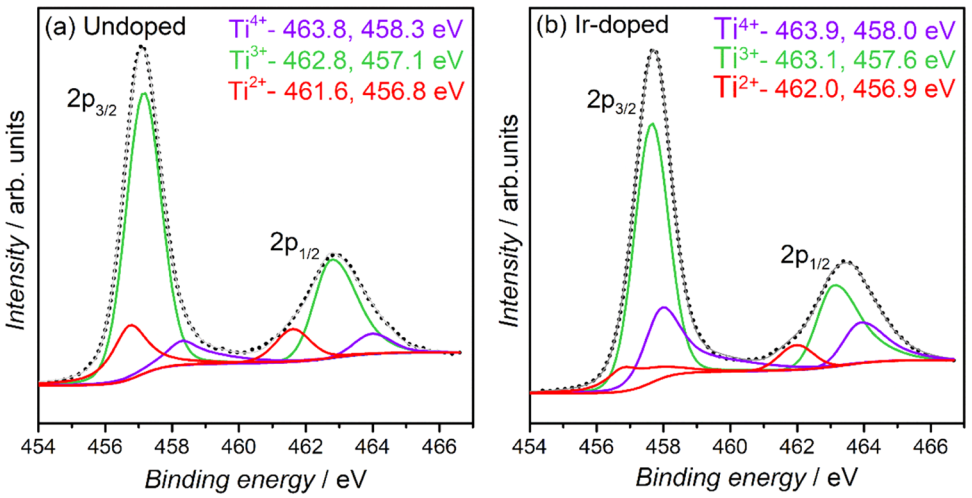

Figure 5. High-resolution XPS Ti 2p core-level spectrum of (a) undoped and (b) Ir-doped BTO.

Table 1. Percentage Composition of Ti^{4+}, Ti^{3+}, and Ti^{2+} in Undoped and Ir-Doped BTO

sample	Ti^{4+} [%]	Ti^{3+} [%]	Ti^{2+} [%]
undoped BTO (FWHM − 1.24)	11	71	18
Ir-doped BTO (FWHM − 1.20)	30	59	11

presence of Ti^{3+}, which is in good agreement with earlier reports.[48,49] The presence of Ti^{2+} is evidenced by peaks at 456.7 eV ($2p_{3/2}$) and 461.6 eV ($2p_{1/2}$).[50] For undoped BTO, Ti exists predominantly (71%) in Ti^{3+} states, endorsing a strong n-type behavior.

Next, the Ti 2p core-level spectra of Ir-doped BTO (Figure 5b) were analyzed. Clearly, the Ti^{4+} signal intensity increased from 11% in undoped BTO to 30% in Ir-doped BTO, as shown in Table 1. The increase of the Ti^{4+} signal on Ir doping is accompanied by a mutual decrease in the signal intensity of lower-valent Ti states (Ti^{3+} and Ti^{2+}), compared to undoped BTO. The relative concentration of the Ti species listed in Table 1 evidenced a factor of 2.6 times increase in the Ti^{4+} concentration upon Ir doping and, consequently, a decrease in the lower-valent Ti^{3+} states. These observations in turn contribute toward the observed p-type behavior for Ir-doped BTO.

XPS data confirmed a decrease in the Ti^{3+} states after Ir doping. By considering stoichiometry, the Ti^{3+} and oxygen vacancies are mutually correlated. If the Ti^{3+} states' concentration is lowered, it naturally accompanies a decrease in oxygen vacancies. However, an XPS study of oxygen vacancies does not offer quantitative information on the different types of oxygen vacancies, which is rather complex. Hence, a spin-sensitive technique such as EPR was used to quantitatively understand the oxygen vacancy concentration change after Ir doping. The EPR technique has been extensively used to reveal a change in the magnitude of the oxygen vacancy in a range of perovskite-based and oxide-type materials.[51,52] Figure 6 compares the EPR spectra of undoped and Ir-doped BTO. It indicates a sharp signal at g = 2.003 corresponding to oxygen vacancies.[25] Compared to undoped BTO, the signal intensity is smaller for Ir-doped BTO, which indicates a decrease in the oxygen vacancy concentration. This notion is further confirmed by a decrement in the corresponding O 1s peak(s) area (O_2 + O_3, corresponding to oxygen vacancies), depicted in Table S3 derived from Figure S2. Thus, a decrease in the Ti^{3+} concentration and also the mutually correlated oxygen vacancy upon Ir doping are confirmed by XPS and EPR analyses, respectively. Changes in the Ba chemical states after Ir doping are discussed in Figure S3.

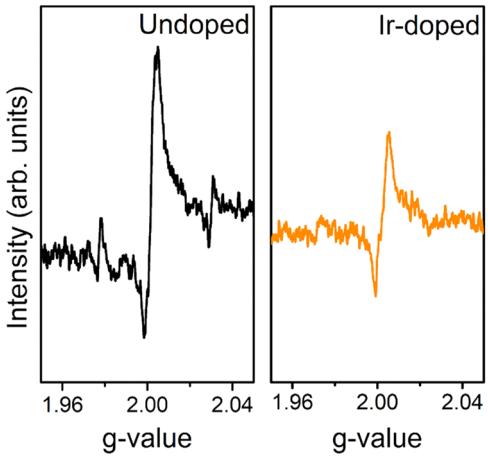

Figure 6. EPR spectra of undoped and Ir-doped BTO with the sharp signal at g = 2.003 corresponding to oxygen vacancies.

In short, collective data from this section revealed that Ir doping occurs at the Ti site of the BTO host lattice. Despite being a bigger sized ion than Ti^{4+}, Ir^{4+} preferentially substituted for Ti sites of the BTO lattice. This observation indicates that deducing information on the site of occupancy solely by considering the ionic radius may not be appropriate. Rather, alternate possibilities like electronegativity or the Goldschmidt tolerance factor[53] are to be considered, which however need further understanding and are beyond the scope of the current study. XPS indicates that Ti exists predominantly as Ti^{3+} in undoped BTO, which renders a strong n-type behavior. However, Ir doping reduces the concentration of Ti^{3+} (also oxygen vacancies) and increases the concentration of Ti^{4+}, suggesting a transition toward p-type behavior. In Section 3.2, the mechanistic origin of doping-induced p-type behavior and visible-light absorption in Ir−BTO will be discussed.

3.2. Origin of Iridium-Doping-Induced Visible-Light Absorption and p-Type Behavior. The optical absorption spectra of undoped BTO and Ir-doped BTO are depicted in

https://doi.org/10.1021/acs.jpcc.3c02942
J. Phys. Chem. C 2023, 127, 12383−12393

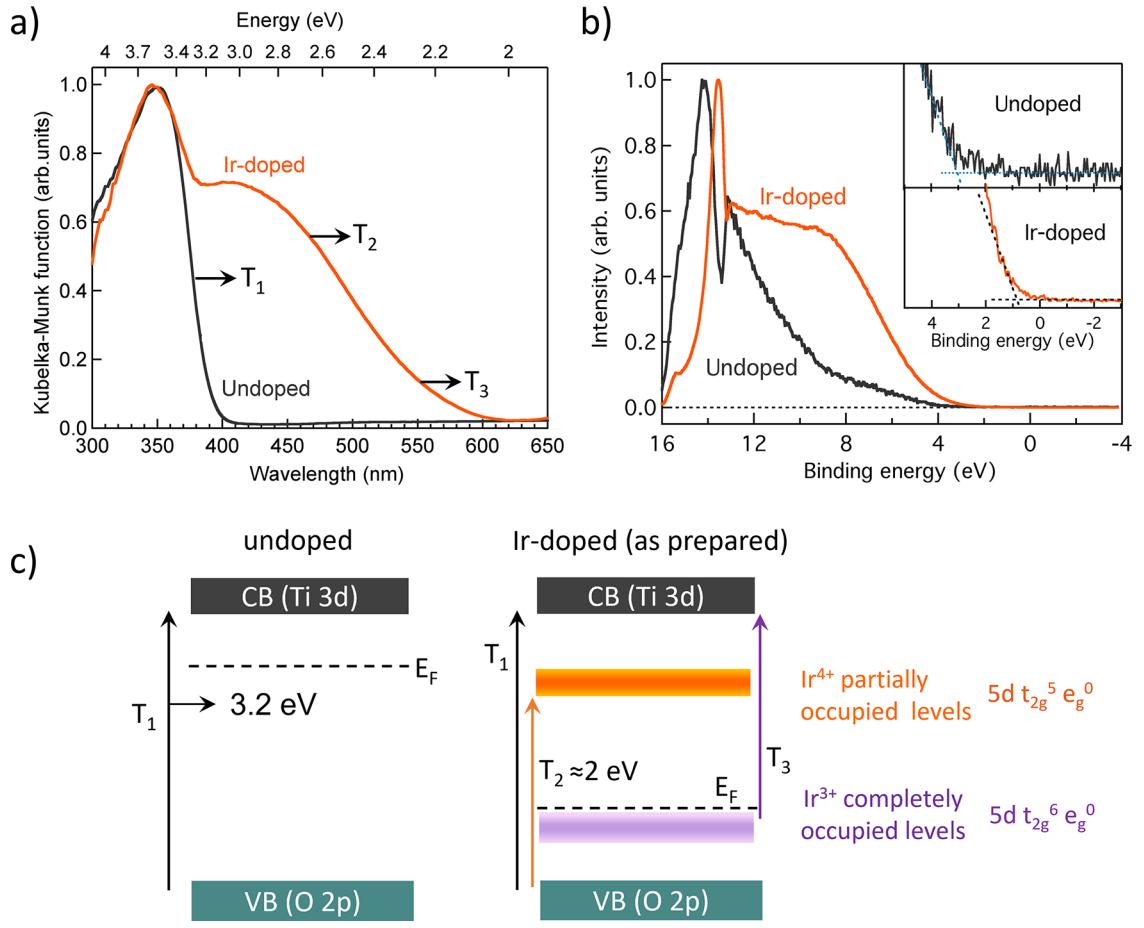

Figure 7. (a) Diffuse reflection spectra from the ultraviolet to the visible region. (b) VB-XPS spectra. (c) Proposed band energy diagram of undoped and Ir-doped BTO.

Figure 7a. The undoped BTO exhibits an absorption onset at around 390 nm, attributed to the fundamental transition from the VB comprising filled O 2p orbitals to the CB consisting of Ti 3d orbitals, indicated as T_1 in Figure 7c.[54] Earlier reports on Ir-doped $SrTiO_3$ red-shifted the optical absorption by introducing interband energy levels compared to its undoped counterpart.[44,55] In BTO, Ir doping exhibits a substantial red shift of optical absorption up to 600 nm, as shown in Figure 7a, which can be ascribed to the formation of Ir-related in-gap energy levels. Therefore, Ir-doped BTO can harvest a wider part of the solar spectra ($\lambda \leq 600$ nm) in comparison to its undoped counterpart, which can absorb only in the UV region.

As revealed by XPS analysis, Ir species existed as Ir^{3+} and Ir^{4+} in the Ir-doped BTO. Ir in its Ir^{4+} state has a partially occupied d^5 electronic configuration (Ir $5d\ t_{2g}^5\ e_g^0$). Thus, electron transition from Ir^{4+} levels to CB Ti 3d orbitals is unlikely. However, electron transition from VB to partially occupied Ir^{4+} levels is feasible. On the other hand, eliciting electron transition from completely occupied Ir^{3+} (Ir $5d\ t_{2g}^6\ e_g^0$) levels to the CB is also possible. Therefore, the absorption band in the region 400−600 nm is attributed to the electron transition either from VB to the partially occupied Ir^{4+} levels, denoted as T_2, or from the completely occupied Ir^{3+} levels to the CB, denoted as T_3 in Figure 7c. However, overlapping contributions make it difficult to distinguish T_2 from T_3 in the optical absorption spectra.

The effect of Ir doping on the Fermi-level position in undoped BTO and Ir-doped BTO was studied by conducting VB-XPS analysis. The shift in the VB onset toward a higher (or lower) binding energy with respect to the undoped sample provides information on the relative changes in the Fermi-level position due to doping. Recently, a VB-XPS study resulted in deducing the p-type behavior after doping $SrTiO_3$ with Al^{3+}.[31] Figure 7b depicts the VB spectra of undoped and Ir-doped BTO with the onset zoomed in the inset. The VB spectral onset of undoped BTO is observed at ≈2.2 eV, indicating that the Fermi level is positioned above the VB edge. Considering the optical band gap of 3.2 eV for the undoped BTO, it can be inferred that the Fermi level is relatively closer to the CB, in agreement with the n-type nature of undoped BTO.[56,57] For the Ir-doped BTO, the VB onset is at ≈0.8 eV, indicating a significant shift of the Fermi level toward the VB edge, compared to the undoped one. This relative Fermi-level downshift after Ir doping indicates a pronounced p-type behavior.

The n- to p-type transition on Ir doping is further corroborated by conducting photoelectrochemical measurements. If Ir doping induces a p-type behavior, a cathodic response in the photocurrent is expected. Indeed, noticing a clear photocathodic current upon light illumination further corroborates the p-type behavior in Ir-doped BTO (Figure S4). A similar approach was earlier used by Kudo et al.[32] and Maeda[33] to ascribe the p-type behavior to perovskite oxides. Besides, Ir-doped BTO shows a visible-light (λ = 427 nm)-responsive photocurrent, corroborating the successful role of Ir doping in extending the optical response of the BTO toward

https://doi.org/10.1021/acs.jpcc.3c02942
J. Phys. Chem. C 2023, 127, 12383−12393

the visible region. Thus, VB-XPS data and photocathodic current infer p-type behavior to Ir-doped BTO.

The plausible mechanisms for the n- to p-type transition in BTO due to Ir doping are discussed as follows. As already discussed using eqs 1 and 2, the n-type nature is ascribed to the Ti^{3+} donor levels, which is also confirmed for undoped BTO by XPS analysis (Figure 5a). Besides, XPS data of Ir doping at Ti sites of BTO (Table 1) showed a factor of 2.6 times increase in the Ti^{4+} concentration upon Ir doping. Concurrently, a decrease in lower-valent Ti^{3+} levels is also observed, which induces a p-type behavior.

To further confirm the effect of Ir doping on the Fermi-level position, computational analysis of the electronic structure is carried out. Figure 8a depicts the DOS of undoped BTO. Here,

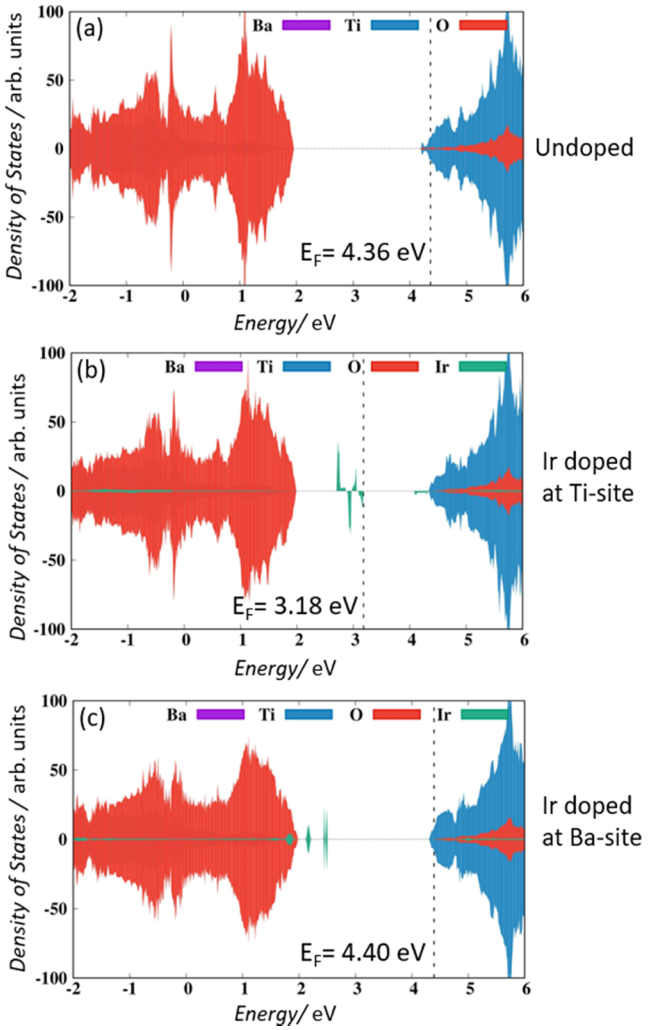

Figure 8. DOS of (a) undoped BTO, (b) Ir-doped BTO with Ir at the Ti site, and (c) DOS of Ir-doped BTO with Ir at the Ba site.

the Fermi level is located close to the CB region, confirming an n-type behavior. Figure 8b presents the DOS of BTO when Ir is doped at the Ti site, and the corresponding DOS of Ir 5d orbitals is depicted in Figure S5. Results in Figure 8b show a substantial downshift (4.36−3.18 eV) of the Fermi level toward the VB, indicating a p-type behavior. This observation is in good agreement with the VB-XPS experimental data (Figure 7b). Note that Ir doping at the Ba site (Figure 8c) did not result in a downward shift of the Fermi level, unlike doping at the Ti site. Therefore, it can be deduced that decreasing the concentration of Ti^{3+} is essential to realize p-type behavior in BTO. This is achieved by preferential doping of Ir at the Ti site, which is clearly evidenced by the XRD, TEM, and XPS data discussed earlier.

Another model to explain the p-type behavior is based on the generation of holes as free charge carriers. The EPR and XPS data in Figures 6 and 5a,b, respectively, demonstrated a reduction in the oxygen vacancy concentration upon Ir doping at the Ti^{4+} site. It means that there is no additional formation of oxygen vacancies after doping. Further, the DOS of Ir 5d orbitals in Ir-doped BTO depicted in Figure S5 indicated the presence of completely occupied and partially occupied levels below and above the Fermi level. This can be related to the coexistence of Ir as Ir^{3+} and Ir^{4+} as discussed in Figure 4. When Ir^{3+} is doped at the Ti^{4+} site, it releases a hole into the system to maintain the charge neutrality (eq 3), thus rendering a p-type behavior. Additionally, the reversible oxidation states of Ir between +3 and +4 in Ir-doped BTO would release holes, further contributing to the p-type behavior, according to eq 4. This is in line with the observation reported for the origin of the p-type behavior in Rh-doped $SrTiO_3$.[32] A decrease in the Ti^{3+} donor-level concentration and hole formation explains the p-type behavior in Ir-doped BTO. Thus, Ir-doped BTO can be a promising p-type perovskite-oxide with visible-light absorption that can be utilized for a range of optoelectronics and photocatalytic applications. We are currently studying the solar hydrogen evolution activity of these samples, which will be reported separately.

$$Ti^{4+} \rightleftharpoons Ir^{3+} + h^{+} \quad (3)$$

$$Ir^{4+} \rightleftharpoons Ir^{3+} + h^{+} \quad (4)$$

To this end, there have been extensive efforts to extend the optical absorption of $ATiO_3$ (A: Ca, Sr, Ba) perovskites via doping of the transition-metal ion. However, there is inadequate information on the fundamental understanding of the origin of dopant-induced optoelectronic properties. Furthermore, the importance of n- to p-type transition in $SrTiO_3$ via aluminum doping has already been demonstrated in view of improving the photocatalytic H_2 evolution efficiency.[29] However, it has been challenging to demonstrate an n- to p-type transition in $ATiO_3$ perovskites simultaneously exhibiting visible-light absorption. Additionally, deducing the dopant site of occupancy solely based on ionic radii of the parent and the dopant cation is impractical as well as challenging owing to the mutual interplay between various parameters. In this work, both of these challenges have been addressed by preferentially doping Ir at the Ti site in BTO. To the best of our knowledge, realizing a p-type behavior with extended optical ($\lambda \leq 600$ nm) absorption using Ir as a dopant is the first of its kind in BTO-based perovskite materials.

4. CONCLUSIONS

Doping Ir at Ti sites of BTO rendered a p-type semiconducting behavior. Collective results from a range of spectroscopy and microscopy investigations in conjunction with computational analysis of the electronic structure confirmed the doping-induced p-type behavior. A red shift in the optical absorption from 390 to 600 nm after doping was attributed to the formation of Ir-related energy levels within the band gap. A systematic correlation of the results offered rational insights into the dopant site of occupancy in the host

https://doi.org/10.1021/acs.jpcc.3c02942
J. Phys. Chem. C 2023, 127, 12383−12393

lattice and the importance of understanding defect chemistry to realize an n- to p-type transition. Ir-doped BTO is an important addition to the very few existing p-type and visible-light-absorbing perovskite oxides, which will find promising applications in optoelectronics and in a range of photocatalytic reactions.

■ ASSOCIATED CONTENT

Supporting Information

The Supporting Information is available free of charge at https://pubs.acs.org/doi/10.1021/acs.jpcc.3c02942.

Calculated lattice parameters from XRD, XPS analysis of Ba and O, Bader charge analysis of undoped and Ir-doped samples, TEM analysis, photoelectrochemical measurements, and DOS plot of Ir 5d orbitals in Ir-doped BTO (PDF)

■ AUTHOR INFORMATION

Corresponding Author

Dharmapura H. K. Murthy − *Department of Chemistry, Manipal Institute of Technology, Manipal Academy of Higher Education, Manipal 576104 Karnataka, India; Center for Renewable Energy, Manipal Institute of Technology, Manipal Academy of Higher Education, Manipal 576104 Karnataka, India;* orcid.org/0000-0003-3462-7269; Email: murthy.dharmapura@manipal.edu

Authors

Sujana Chandrappa − *Department of Chemistry, Manipal Institute of Technology, Manipal Academy of Higher Education, Manipal 576104 Karnataka, India*

Simon Joyson Galbao − *Department of Chemistry, Manipal Institute of Technology, Manipal Academy of Higher Education, Manipal 576104 Karnataka, India*

P. S. Sankara Rama Krishnan − *School of Materials Science and Engineering, Nanyang Technological University, 639798, Singapore;* orcid.org/0000-0003-3890-8543

Namitha Anna Koshi − *Indo-Korea Science and Technology Center (IKST), Bengaluru 560065, India*

Srewashi Das − *Department of Chemistry, Indian Institute of Technology Bombay, Mumbai 400076, India*

Stephen Nagaraju Myakala − *Institute of Materials Chemistry, Technische Universität Wien, 1060 Vienna, Austria;* orcid.org/0000-0001-7234-6252

Seung-Cheol Lee − *Indo-Korea Science and Technology Center (IKST), Bengaluru 560065, India;* orcid.org/0000-0002-9741-6955

Arnab Dutta − *Department of Chemistry, Indian Institute of Technology Bombay, Mumbai 400076, India;* orcid.org/0000-0002-9998-6329

Alexey Cherevan − *Institute of Materials Chemistry, Technische Universität Wien, 1060 Vienna, Austria;* orcid.org/0000-0001-8934-6371

Satadeep Bhattacharjee − *Indo-Korea Science and Technology Center (IKST), Bengaluru 560065, India;* orcid.org/0000-0002-6717-2881

Complete contact information is available at: https://pubs.acs.org/10.1021/acs.jpcc.3c02942

Author Contributions

The manuscript was written through contributions of all authors. All authors have given approval to the final version of the manuscript.

Notes

The authors declare no competing financial interest.

■ ACKNOWLEDGMENTS

S.C. and D.H.K.M. acknowledge the Technology Mission Division (Energy, Water & all Others), the Department of Science & Technology, Ministry of Science & Technology, Government of India, Reference Number DST/TMD/IC-MAP/2K20/02, project titled as Integrated Clean Energy Material Acceleration Platform (IC-MAP) on Bioenergy and Hydrogen. D.H.K.M. would like to thank Dr. Nagaraja K. K. and Dr. Mallikarjun Bhavanari for their comments on the manuscript.

■ REFERENCES

(1) Karvounis, A.; Timpu, F.; Vogler-Neuling, V. V.; Savo, R.; Grange, R. BaTiO 3: Barium Titanate Nanostructures and Thin Films for Photonics. *Adv. Opt. Mater.* **2020**, *8*, No. 2070094.

(2) Park, K.; Seo, D. Gas Sensing Characteristics of BaTiO3-Based Ceramics. *Mater. Chem. Phys.* **2004**, *85*, 47−51.

(3) Shoron, O. F.; Raghavan, S.; Freeze, C. R.; Stemmer, S. BaTiO3 /SrTiO3 Heterostructures for Ferroelectric Field Effect Transistors. *Appl. Phys. Lett.* **2017**, *110*, No. 232902.

(4) Srilakshmi, C.; Rao, G. M.; Saraf, R. Effect of the Nature of a Transition Metal Dopant in BaTiO 3 Perovskite on the Catalytic Reduction of Nitrobenzene. *RSC Adv.* **2015**, *5*, 45965−45973.

(5) Tang, Q.; Wu, J.; Kim, D.; Franco, C.; Terzopoulou, A.; Veciana, A.; Puigmartí-Luis, J.; Chen, X.; Nelson, B. J.; Pané, S. Enhanced Piezocatalytic Performance of BaTiO 3 Nanosheets with Highly Exposed {001} Facets. *Adv. Funct. Mater.* **2022**, *32*, No. 2202180.

(6) Yacout, N.; Refai, H. S.; Kebede, M. A.; Salman, F.; Sheha, E. Significant Study of BaTiO3 as a Cathode for Magnesium Battery Applications. *Mater. Chem. Phys.* **2022**, *292*, No. 126770.

(7) Banakhojasteh, S.; Beckert, S.; Gläser, R. Modification of SrTiO3 as a Photocatalyst for Hydrogen Evolution from Aqueous Methanol Solution. *J. Photochem. Photobiol. A* **2018**, *366*, 48−54.

(8) Nishioka, S.; Maeda, K. Hydrothermal Synthesis of Rhodium-Doped Barium Titanate Nanocrystals for Enhanced Photocatalytic Hydrogen Evolution under Visible Light. *RSC Adv.* **2015**, *5*, 100123−100128.

(9) Karthik, K. V.; Reddy, C. V.; Reddy, K. R.; Ravishankar, R.; Sanjeev, G.; Kulkarni, R. V.; Shetti, N. P.; Raghu, A. V. Barium Titanate Nanostructures for Photocatalytic Hydrogen Generation and Photodegradation of Chemical Pollutants. *J. Mater. Sci. Mater. Electron.* **2019**, *30*, 20646−20653.

(10) Michel, V. F.; Esswein, T.; Spaldin, N. A. Interplay between Ferroelectricity and Metallicity in BaTiO 3. *J. Mater. Chem. C* **2021**, *9*, 8640−8649.

(11) Freeman, C. L.; Dawson, J. A.; Chen, H.-R.; Ben, L.; Harding, J. H.; Morrison, F. D.; Sinclair, D. C.; West, A. R. Energetics of Donor-Doping, Metal Vacancies, and Oxygen-Loss in A-Site Rare-Earth-Doped BaTiO3. *Adv. Funct. Mater.* **2013**, *23*, 3925−3928.

(12) Ramakanth, S.; Hamad, S.; Venugopal Rao, S.; James Raju, K. C. Magnetic and Nonlinear Optical Properties of BaTiO 3 Nanoparticles. *AIP Adv.* **2015**, *5*, No. 057139.

(13) Nedumkandathil, R.; Jaworski, A.; Grins, J.; Bernin, D.; Karlsson, M.; Eklöf-Österberg, C.; Neagu, A.; Tai, C.-W.; Pell, A. J.; Häussermann, U. Hydride Reduction of BaTiO3− Oxyhydride Versus O Vacancy Formation. *ACS Omega* **2018**, *3*, 11426−11438.

(14) Chan, N.-H.; Sharma, R. K.; Smyth, D. M. Nonstoichiometry in Undoped BaTiO3. *J. Am. Ceram. Soc.* **1981**, *64*, 556−562.

(15) Scharfschwerdt, R.; Mazur, A.; Schirmer, O. F.; Hesse, H.; Mendricks, S. Oxygen Vacancies in BaTiO3. *Phys. Rev. B* **1996**, *54*, 15284−15290.
(16) Tian, X.; Brennecka, G. L.; Tan, X. Structural Instability in Electrically Stressed, Oxygen Deficient BaTiO3 Nanocrystals. *Adv. Funct. Mater.* **2020**, *30*, No. 2004607.
(17) Amano, F.; Nakata, M.; Yamamoto, A.; Tanaka, T. Effect of Ti 3+ Ions and Conduction Band Electrons on Photocatalytic and Photoelectrochemical Activity of Rutile Titania for Water Oxidation. *J. Phys. Chem. C* **2016**, *120*, 6467−6474.
(18) Di Valentin, C.; Pacchioni, G.; Selloni, A. Reduced and N-Type Doped TiO 2: Nature of Ti3+ Species. *J. Phys. Chem. C* **2009**, *113*, 20543−20552.
(19) Nowotny, J. Defect Chemistry of BaTiO3. *Solid State Ionics* **1991**, *49*, 135−154.
(20) Sinclair, D. C.; West, A. R. Impedance and Modulus Spectroscopy of Semiconducting BaTiO 3 Showing Positive Temperature Coefficient of Resistance. *J. Appl. Phys.* **1989**, *66*, 3850−3856.
(21) Panthi, G.; Park, M. Approaches for Enhancing the Photocatalytic Activities of Barium Titanate: A Review. *J. Energy Chem.* **2022**, *73*, 160−188.
(22) Upadhyay, S.; Shrivastava, J.; Solanki, A.; Choudhary, S.; Sharma, V.; Kumar, P.; Singh, N.; Satsangi, V. R.; Shrivastav, R.; Waghmare, U. V.; Dass, S. Enhanced Photoelectrochemical Response of BaTiO 3 with Fe Doping: Experiments and First-Principles Analysis. *J. Phys. Chem. C* **2011**, *115*, 24373−24380.
(23) Yang, C.; Chen, Y.; Chen, T.; Rajendran, S.; Zeng, Z.; Qin, J.; Zhang, X. A Long-Standing Polarized Electric Field in TiO2@ BaTiO3/CdS Nanocomposite for Effective Photocatalytic Hydrogen Evolution. *Fuel* **2022**, *314*, No. 122758.
(24) Li, H.; Song, Y.; Zhang, J.; He, J. Turbulence Enhanced Ferroelectric-Nanocrystal-Based Photocatalysis in Urchin-like TiO2 /BaTiO3 Microspheres for Hydrogen Evolution. *Nanoscale Adv.* **2021**, *3*, 5618−5625.
(25) Jiang, Y.; Toe, C. Y.; Mofarah, S. S.; Cazorla, C.; Chang, S. L. Y.; Yin, Y.; Zhang, Q.; Lim, S.; Yao, Y.; Tian, R.; et al. Efficient Cocatalyst-Free Piezo-Photocatalytic Hydrogen Evolution of Defective BaTiO3− x Nanoparticles from Seawater. *ACS Sustainable Chem. Eng.* **2023**, *11*, 3370−3389.
(26) Yu, C.; He, J.; Tan, M.; Hou, Y.; Zeng, H.; Liu, C.; Meng, H.; Su, Y.; Qiao, L.; Lookman, T.; Bai, Y. Selective Enhancement of Photo-Piezocatalytic Performance in BaTiO3 Via Heterovalent Ion Doping. *Adv. Funct. Mater.* **2022**, *32*, No. 2209365.
(27) Lei, Y.; Xu, S.; Ding, M.; Li, L.; Sun, Q.; Wang, Z. L. Enhanced Photocatalysis by Synergistic Piezotronic Effect and Exciton−Plasmon Interaction Based on (Ag-Ag2 S)/BaTiO3 Heterostructures. *Adv. Funct. Mater.* **2020**, *30*, No. 2005716.
(28) Nishiyama, H.; Yamada, T.; Nakabayashi, M.; Maehara, Y.; Yamaguchi, M.; Kuromiya, Y.; Nagatsuma, Y.; Tokudome, H.; Akiyama, S.; Watanabe, T.; et al. Photocatalytic Solar Hydrogen Production from Water on a 100-m2 Scale. *Nature* **2021**, *598*, 304−307.
(29) Ham, Y.; Hisatomi, T.; Goto, Y.; Moriya, Y.; Sakata, Y.; Yamakata, A.; Kubota, J.; Domen, K. Flux-Mediated Doping of SrTiO3 Photocatalysts for Efficient Overall Water Splitting. *J. Mater. Chem. A* **2016**, *4*, 3027−3033.
(30) Takata, T.; Domen, K. Defect Engineering of Photocatalysts by Doping of Aliovalent Metal Cations for Efficient Water Splitting. *J. Phys. Chem. C* **2009**, *113*, 19386−19388.
(31) Zhao, Z.; Goncalves, R. V.; Barman, S. K.; Willard, E. J.; Byle, E.; Perry, R.; Wu, Z.; Huda, M. N.; Moulé, A. J.; Osterloh, F. E. Electronic Structure Basis for Enhanced Overall Water Splitting Photocatalysis with Aluminum Doped SrTiO3 in Natural Sunlight. *Energy Environ. Sci.* **2019**, *12*, 1385−1395.
(32) Iwashina, K.; Kudo, A. Rh-Doped SrTiO3 Photocatalyst Electrode Showing Cathodic Photocurrent for Water Splitting under Visible-Light Irradiation. *J. Am. Chem. Soc.* **2011**, *133*, 13272−13275.
(33) Maeda, K. Rhodium-Doped Barium Titanate Perovskite as a Stable p-Type Semiconductor Photocatalyst for Hydrogen Evolution under Visible Light. *ACS Appl. Mater. Interfaces* **2014**, *6*, 2167−2173.
(34) Murthy, D. H. K.; Matsuzaki, H.; Wang, Q.; Suzuki, Y.; Seki, K.; Hisatomi, T.; Yamada, T.; Kudo, A.; Domen, K.; Furube, A. Revealing the Role of the Rh Valence State, La Doping Level and Ru Cocatalyst in Determining the H2 Evolution Efficiency in Doped SrTiO3 Photocatalysts. *Sustainable Energy Fuels* **2019**, *3*, 208−218.
(35) Kato, H.; Sasaki, Y.; Shirakura, N.; Kudo, A. Synthesis of Highly Active Rhodium-Doped SrTiO3 Powders in Z-Scheme Systems for Visible-Light-Driven Photocatalytic Overall Water Splitting. *J. Mater. Chem. A* **2013**, *1*, 12327−12333.
(36) Wang, Q.; Hisatomi, T.; Jia, Q.; Tokudome, H.; Zhong, M.; Wang, C.; Pan, Z.; Takata, T.; Nakabayashi, M.; Shibata, N.; et al. Scalable Water Splitting on Particulate Photocatalyst Sheets with a Solar-to-Hydrogen Energy Conversion Efficiency Exceeding 1%. *Nat. Mater.* **2016**, *15*, 611−615.
(37) Jia, Q.; Iwase, A.; Kudo, A. BiVO4−Ru/SrTiO3:Rh Composite Z-Scheme Photocatalyst for Solar Water Splitting. *Chem. Sci.* **2014**, *5*, 1513.
(38) Bhat, D. K.; Bantawal, H.; Shenoy, U. S. Rhodium Doping Augments Photocatalytic Activity of Barium Titanate: Effect of Electronic Structure Engineering. *Nanoscale Adv.* **2020**, *2*, 5688−5698.
(39) Corà, F.; Catlow, C. R. A. QM Investigations on Perovskite-Structured Transition Metal Oxides: Bulk, Surfaces and Interfaces. *Faraday Discuss.* **1999**, *114*, 421−442.
(40) Williams, D. B.; Carter, C. B. *Transmission Electron Microscopy*; Springer: Boston, MA, 2009.
(41) Sohlberg, K.; Pennycook, T. J.; Zhou, W.; Pennycook, S. J. Insights into the Physical Chemistry of Materials from Advances in HAADF-STEM. *Phys. Chem. Chem. Phys.* **2015**, *17*, 3982−4006.
(42) Liu, Y.; Huang, H.; Xue, L.; Sun, J.; Wang, X.; Xiong, P.; Zhu, J. Recent Advances in the Heteroatom Doping of Perovskite Oxides for Efficient Electrocatalytic Reactions. *Nanoscale* **2021**, *13*, 19840−19856.
(43) Dai, J.; Zhu, Y.; Tahini, H. A.; Lin, Q.; Chen, Y.; Guan, D.; Zhou, C.; Hu, Z.; Lin, H.-J.; Chan, T.-S.; et al. Single-Phase Perovskite Oxide with Super-Exchange Induced Atomic-Scale Synergistic Active Centers Enables Ultrafast Hydrogen Evolution. *Nat. Commun.* **2020**, *11*, No. 5657.
(44) Kawasaki, S.; Takahashi, R.; Akagi, K.; Yoshinobu, J.; Komori, F.; Horiba, K.; Kumigashira, H.; Iwashina, K.; Kudo, A.; Lippmaa, M. Electronic Structure and Photoelectrochemical Properties of an Ir-Doped SrTiO3 Photocatalyst. *J. Phys. Chem. C* **2014**, *118*, 20222−20228.
(45) da Silva, L.; Alves, V.; de Castro, S.; Boodts, J. F. XPS Study of the State of Iridium, Platinum, Titanium and Oxygen in Thermally Formed IrO2+TiO2+PtOX Films. *Colloids Surf., A* **2000**, *170*, 119−126.
(46) Ardizzone, S.; Bianchi, C. L.; Cappelletti, G.; Ionita, M.; Minguzzi, A.; Rondinini, S.; Vertova, A. Composite Ternary SnO2−IrO2−Ta2O5 Oxide Electrocatalysts. *J. Electroanal. Chem.* **2006**, *589*, 160−166.
(47) Spasojevic, I.; Sauthier, G.; Caicedo, J. M.; Verdaguer, A.; Domingo, N. Oxidation Processes at the Surface of BaTiO3 Thin Films under Environmental Conditions. *Appl. Surf. Sci.* **2021**, *565*, No. 150288.
(48) Zheng, Z. Q.; Zhou, X. P. Reduction of Ti 4+ to Ti 3+ in Boron-Doped BaTiO 3 at Very Low Temperature. *J. Am. Ceram. Soc.* **2013**, *96*, 3504−3510.
(49) Zhang, Q.; Zhai, J.; Ben, Q.; Yu, X.; Yao, X. Enhanced Microwave Dielectric Properties of Ba0.4Sr0.6TiO3 Ceramics Doping by Metal Fe Powders. *J. Appl. Phys.* **2012**, *112*, No. 104104.
(50) Wu, Q.; Zhang, C.; Zhang, B.; Li, X.; Ying, Z.; Liu, T.; Lin, W.; Yu, Y.; Cheng, H.; Zhao, F. Highly Selective Pt/Ordered Mesoporous TiO2−SiO2 Catalysts for Hydrogenation of Cinnamaldehyde: The Promoting Role of Ti2+. *J. Colloid Interface Sci.* **2016**, *463*, 75−82.

https://doi.org/10.1021/acs.jpcc.3c02942
J. Phys. Chem. C 2023, 127, 12383−12393

(51) Xue, J.; Zhu, X.; Zhang, Y.; Wang, W.; Xie, W.; Zhou, J.; Bao, J.; Luo, Y.; Gao, X.; Wang, Y.; et al. Nature of Conduction Band Tailing in Hydrogenated Titanium Dioxide for Photocatalytic Hydrogen Evolution. *ChemCatChem* **2016**, *8*, 2010−2014.
(52) Shah, M. W.; Zhu, Y.; Fan, X.; Zhao, J.; Li, Y.; Asim, S.; Wang, C. Facile Synthesis of Defective TiO2−x Nanocrystals with High Surface Area and Tailoring Bandgap for Visible-Light Photocatalysis. *Sci. Rep.* **2015**, *5*, No. 15804.
(53) Bartel, C. J.; Sutton, C.; Goldsmith, B. R.; Ouyang, R.; Musgrave, C. B.; Ghiringhelli, L. M.; Scheffler, M. New Tolerance Factor to Predict the Stability of Perovskite Oxides and Halides. *Sci. Adv.* **2019**, *5*, No. eaav0693.
(54) Yang, F.; Yang, L.; Ai, C.; Xie, P.; Lin, S.; Wang, C.-Z.; Lu, X. Tailoring Bandgap of Perovskite BaTiO3 by Transition Metals Co-Doping for Visible-Light Photoelectrical Applications: A First-Principles Study. *Nanomaterials* **2018**, *8*, 455.
(55) Suzuki, S.; Matsumoto, H.; Iwase, A.; Kudo, A. Enhanced H 2 Evolution over an Ir-Doped SrTiO3 Photocatalyst by Loading of an Ir Cocatalyst Using Visible Light up to 800 Nm. *Chem. Commun.* **2018**, *54*, 10606−10609.
(56) Schafranek, R.; Baniecki, J. D.; Ishii, M.; Kotaka, Y.; Kurihara, K. The SrTiO 3 /BiFeO 3 (001) Interface: Commutativity of Energy Band Discontinuities. *New J. Phys.* **2013**, *15*, No. 053014.
(57) Chavarría, C. C.; Payan, S.; Salvetat, J.-P.; Maglione, M.; Klein, A. Fermi Level Engineering for Large Permittivity in BaTiO3-Based Multilayers. *Surfaces* **2020**, *3*, 567−578.
(58) Kresse, G.; Furthmüller, J. Efficiency of Ab-Initio Total Energy Calculations for Metals and Semiconductors Using a Plane-Wave Basis Set. *Comput. Mater. Sci.* **1996**, *6*, 15−50.
(59) Kresse, G.; Furthmüller, J. Efficient Iterative Schemes for Ab Initio Total-Energy Calculations Using a Plane-Wave Basis Set. *Phys. Rev. B* **1996**, *54*, 11169−11186.
(60) Kresse, G.; Joubert, D. From Ultrasoft Pseudopotentials to the Projector Augmented-Wave Method. *Phys. Rev. B* **1999**, *59*, 1758−1775.
(61) Blöchl, P. E. Projector Augmented-Wave Method. *Phys. Rev. B* **1994**, *50*, 17953−17979.
(62) Perdew, J. P.; Burke, K.; Ernzerhof, M. Generalized Gradient Approximation Made Simple. *Phys. Rev. Lett.* **1996**, *77*, 3865−3868.
(63) Monkhorst, H. J.; Pack, J. D. Special Points for Brillouin-Zone Integrations. *Phys. Rev. B* **1976**, *13*, 5188−5192.
(64) Dudarev, S. L.; Botton, G. A.; Savrasov, S. Y.; Humphreys, C. J.; Sutton, A. P. Electron-Energy-Loss Spectra and the Structural Stability of Nickel Oxide: An LSDA+U Study. *Phys. Rev. B* **1998**, *57*, 1505−1509.
(65) Tymińska, N.; Wu, G.; Dupuis, M. Water Oxidation on Oxygen-Deficient Barium Titanate: A First-Principles Study. *J. Phys. Chem. C* **2017**, *121*, 8378−8389.

https://doi.org/10.1021/acs.jpcc.3c02942
J. Phys. Chem. C 2023, 127, 12383−12393